Supporting Information

Ponce-Alvarez et al. 10.1073/pnas.1300098110

SI Methods

Initial Basic Analysis and Inclusion Criteria. We analyzed the spiking activity of single neurons and pairs of simultaneously recorded neurons if at least 15 trials per stimulus condition were recorded. We calculated the mean number of spikes within two analysis windows (150–650 ms after stimulus onset for stimulus driven activity, 500–0 ms before stimulus onset for the spontaneous activity) and determined the direction of motion that yielded the highest activity level (labeled preferred direction, PD) and the activity with stimuli moving opposite to the PD (null direction, NULL). We then calculated a direction index (DI = 1–(NULL/PD) after subtraction of spontaneous activity). Only cells that had a DI > 0.5 were included in the study. In the case of noise correlation calculation, both cells had to have a DI > 0.5. We then assessed whether the activity measured with any of the different directions of motion showed monotonic changes over time, as this would be indicative of slow drifts, possibly due to a deterioration of recording quality that would affect our data. We did this by calculating the Pearson correlation coefficient associated with a given direction of motion using trial number (i.e., time) as our independent variable. This yielded 32 correlation coefficients (14 coefficients in the case of the contrast experiments). If any of these had a P value smaller than 0.05/32 (0.05/14 for the contrast experiments, respectively, accounting for multiple comparisons), the cell was excluded from further analysis, as a slow drift was present. For cells to be included into the noise correlation analysis, both neurons had to show a DI > 0.5, and their PD had to be within 45°, and neither showed evidence of slow drifts. For this analysis the PD was assessed differently than described above (DI calculation). Namely, based on the activities associated with all eight directions of motion, we calculated the PD vector according to:

$$X = \sum_{i=1}^{8} \sin\left(\frac{\pi}{4}i - \frac{\pi}{4}\right).act_i \qquad \text{[S1]}$$

and

$$Y = \sum_{i=1}^{8} \cos\left(\frac{\pi}{4}i - \frac{\pi}{4}\right).act_i, \qquad \text{[S2]}$$

whereby act_i represents the activity associated with a given direction of motion elicited by a grating stimulus, and i corresponds to the eight different directions of motion. X and Y are the vector components in polar coordinates, from which the vector angle was calculated. If the vector angles for the two recorded cells were within 45° from one another, the cells were analyzed further.

Single Cell Example. Fig. S1 shows the spiking activity of an example single neuron. Fig. S1*A* displays the spiking activity and associated firing rate for stimuli moving in different directions. The resolved Fano factor (FF) for the different stimulus types is shown in Fig. S1*B*. Note that the example cell presents most of the characteristics of the population activity, albeit in a noisier way.

Pooling Across Different Neuronal Response Types. The middle temporal (MT) visual area contains pattern and component cells, which exhibit different responses when confronted with plaid stimuli. Pattern cells respond with a very similar tuning curve to grating and plaid stimuli, whereas component cells show typically some bilobed tuning when confronted with plaid stimuli, as they respond most strongly when one of the plaid components moves in PD. Thus, the various plaid stimuli used in the direction of motion experiment drive component and pattern cells differently. It might therefore be argued that the tuning of the FFs and noise correlation is largely due to the responses from, for example, component cells (e.g., due to the bilobed responses/tuning curve, or vice versa from pattern cells because of the lack of it). However, the argument of different tuning curves does not apply to conditions when the grating stimulus was presented. Importantly we also show the FF tuning for the grating stimulus condition. Thus, the effect seen in our data cannot be explained by assuming that there was different stimulus drive in pattern and component cells when plaid stimuli were presented.

Our rationale for pooling pattern and component (and unclassified cells) is also based on the fact that MT cells form a continuum from pattern to unclassified to component cells. Unclassified cells constitute at least one-third of the population when using 135 degrees (deg) plaids (as used in our experiments). If we subdivided our sample into groups of ∼one-third (component, unclassified/ pattern), we would end up with ∼14 cells in each group, which does not allow for meaningful analysis of population tuning pattern. Finally, if component cells did behave differently from pattern cells, and one group did not show the type of tuning we report here, then it would mean that the other group shows the tuning even more prominently.

We nevertheless assessed whether FF tuning might differ between extremes of the component–pattern classification. To this end we calculated the component pattern index (CPI) for each cell, and rank ordered these indices. We first calculated the partial correlation for the pattern and component predictions as previously described (1), using the activity in the response window from 150 to 650 ms after stimulus onset. The pattern and component predictions (Rp and Rc) are calculated as follows:

$$R_p = \frac{r_p - r_c * r_{pc}}{\sqrt{\left(1 - r_c^2\right) * \left(1 - r_{pc}^2\right)}}$$

and

$$R_c = \frac{r_c - r_p * r_{pc}}{\sqrt{\left(1 - r_p^2\right) * \left(1 - r_{pc}^2\right)}},$$

whereby r_p is the correlation of the data with the pattern prediction, r_c is the correlation of the data with the component prediction, and r_{pc} is the correlation between the two predictions.

The CPI is then calculated as:

$$CPI = \frac{R_c - R_p}{2}.$$

More negative values indicate that cells were more pattern-like and positive values the opposite. We are aware that our stimuli were not ideally suited to make the pattern component classification, as they were not sinusoidal stimuli. Therefore, plaid stimuli had motion energy in directions intermediate to the component motion (to a various degree depending on the plaid; intentionally so). To avoid dependence of the CPI on the different plaid patterns, we used the noncoherent plaid responses to calculate the CPI.

We rank ordered the CPI and subdivided our data into three groups of 10 cells each. One group consisted of the 10 cells with the lowest CPIs (most pattern-like), one group covered the middle ground (median 10 CPIs)—that is, they were least classified in terms of component–pattern cell type—and finally a group consisted of 10 cells with the largest CPIs (most component-like). Note that this classification does not mean the cells in the pattern-like or component-like groups were genuine pattern or component cells, as a different classification would be needed to make that classification.

We then calculated the FF tuning for these three groups when the grating stimulus was presented. The results are shown in Fig. S2. From the figure it appears that M-shaped variance tuning is present in all three cell classes. Visual inspection suggests that the least classified cell group shows the strongest tuning, but the other cell groups equally show some evidence of M-shaped tuning. The tuning in neither of the cell groups individually was significant, but that is likely due to the small sample size available for this breakdown.

Nonnormalized Population Activity. Fig. S3 presents the nonnormalized mean population activity for different stimulus directions and for each stimulus type. Neuronal activity peaks around the PD. For anti-PDs 50% of the cells (21 of 42) significantly decrease the firing rate with respect to its baseline level (t test, $P < 0.05$), a feature that is captured by the computational model.

Nonnormalized Variance. Fig. S4 presents the nonnormalized population variance for different stimulus directions and for each stimulus type. For comparison, the total variance predicted by the model is also shown. Note that, in the computational stochastic model, we concentrate on the statistics of the underlying firing rate and assume that spikes are generated via a Poisson process. Thus, the variance of the underlying rate adds an extra variability to the one expected for a Poisson process (for which the variance equals the rate). This is supported by the observation that empirical FFs are >1—that is, more variable than a homogenous Poisson process. The excess of variance is shown in Fig. 1*B*, as measure by the FF. As shown in the main text, in both the data and the model, the extra variability is higher for intermediated direction preferences (as shown in Fig. 1*B* and Fig. 5 *D* and *I*).

Neuronal Tuning to Contrast Modulated Stimuli. We tested whether the tuning of the FF could reflect a nonlinear relationship between variance and mean firing rate rather than direction tuning per se. For this, we investigated the tuning of MT neurons to moving stimuli of different contrasts (Fig. S5; see also Fig. 1 *D–F*). We analyzed the FF and the firing rate variations in a dataset (50 single cells) where the luminance contrast of sinewave gratings was systematically manipulated. These either moved in preferred or antipreferred motion direction. FFs decreased as stimulus contrast increased for both preferred and antipreferred motion directions. Importantly, the FF changes were monotonic throughout: there was no increase of FFs at intermediate firing rates. Thus, the tuning of FF found for different motion directions is not a by-product of a nonlinear dependence between FF and firing rate that makes FFs higher for intermediate firing rates.

Contrast Manipulation. In our contrast experiment, animals fixated a small target as described above during a 500-ms prestimulus and a 1,000-ms stimulus period. Visual stimuli were generated using a Sergent Pepper Graphics board (Number Nine Computer Corp.: 640 × 480 pixel resolution, 60 Hz frame rate) residing in a Pentium-based PC, and were displayed on a 20-inch analog red-green-blue (RGB) monitor (Sony GDM 2000TC, 60 Hz, noninterlaced). The outputs of the red and green guns were combined, such that a resolution of 12 bits per pixel was achieved (2). This manipulation allowed for the presentation of contrasts on the monitor that were low enough to obtain luminance contrast thresholds (see refs. 3, 4 for additional details). Luminance contrasts used were 0.25%, 0.5%, 1.0%, 2.0%, 4.0%, 8.0%, and 16.0% (Michelson contrast).

Calculation of Trial-by-Trial Spike Count (Noise) Correlation. For each stimulus condition we determined the number of spikes elicited by neuron 1, and the number of spikes elicited by neuron 2 and calculated the sample correlation coefficient r_c according to:

$$r_c = \frac{\sum_{i=1}^{n}(x_i - \langle x\rangle)(y_i - \langle y\rangle)}{\sqrt{\sum_{i=1}^{n}(x_i - \langle x\rangle)^2 \sum_{i=1}^{n}(y_i - \langle y\rangle)^2}}, \qquad \text{[S3]}$$

where x_i and y_i are the spike counts of each neuron on trial i, $<x>$ and $<y>$ are the corresponding sample means, and n is the number of trials recorded. The correlation was corrected by subtracting the shift–predictor correlation, which is simply the correlation (as calculated above) between the activity recorded from neuron 1 for trial $i = 1, 2, \ldots, n–1$ and from neuron 2 in trial $j = i+1 = 2, 3, \ldots, n$, whereby trial $i = n$ in neuron 1 was paired with trial $j = 1$ in neuron 2.

Spike Sorting. Action potentials of single neurons were isolated using an Alpha-Omega online spike sorter, whereby a template-matching algorithm generated error histograms (EHs) for each spike. Unimodal EH with the far flank of the distribution returning to baseline was an indication of a perfectly isolated cell. We only included cells that fulfilled this criterion (as assessed online). We did not store the waveforms at the time of recording.

Computational Model. We studied the dynamics of M interconnected populations of neurons using the following rate-based model. Within this model, each neuron transforms rate inputs (u) into an output rate (r). The dynamics are given by the following Langevin equation:

$$\tau_m \frac{dr_i^m(t)}{dt} = -r_i^m(t) + H\left[u_i^m(t)\right] + \xi_i(t), \qquad \text{[S4]}$$

$$u_i^m(t) = \frac{w_{mm}}{N_m - 1}\sum_{j\neq i} r_j^m(t) + \sum_{n\neq m}\frac{w_{mn}}{(M-1)N_n}\sum_j r_j^n(t) + I_m(t), \qquad \text{[S5]}$$

and

$$H(u) = \tanh\left(\frac{u}{a}\right)\Theta(u), \qquad \text{[S6]}$$

where $r_i^m(t)$ is the firing rate of unit i ($1 \le i \le N_m$) from population m ($1 \le m \le M$), N_m is the size of population m, and M the number of populations. $H(u)$ is the transfer function of the neurons, with $\Theta(u)$ being the unit step Heaviside function. The parameter a controls the gain of H, and it is set to $a = 10$. The saturating behavior of H captures the effect of refractoriness of biological neurons. The neurons are all-to-all connected by a connectivity matrix $W = \{w_{mn}\}$, where w_{mn} is the coupling between neurons from population m and n. Intrinsic noise, $\xi_i(t)$, is additive and white:

$$\langle \xi_i(t)\rangle = 0 \;;\; \langle \xi_i(t)\xi_j(t')\rangle = \beta^2\delta_{ij}\delta(t-t'), \qquad \text{[S7]}$$

where the angular brackets <.> denote the average over realizations and δ_{ij} is the Kronecker's delta symbol.

All neurons from a given population receive an external input $I_m(t)$ to which input extrinsic noise, δI, is added and is given by:

$$\langle \delta I_i(t) \rangle = 0 \;;\; \langle \delta I_i(t) \delta I_j(t') \rangle = \beta_I^2 \delta_{ij} \delta(t-t'). \qquad \textbf{[S8]}$$

Here we assume that the extrinsic noise is sufficiently small, so that, after Taylor expansion, Eq. **S4** can be written as: $\tau_m \dot{r}_i^m = -r_i^m + H[u_i^m] + \frac{\partial H(u_m)}{\partial u} \delta I_i + \xi_i$.

For simplicity, we set $\tau_m = 1$. Thus, the unit of time is the time scale of the rate of all neurons that is assumed to be equal to 10 ms. To get firing rates in the range of biological neurons, we multiply the rate variables by 60.

We studied a model in which M neural populations are arranged on a ring, so that they are labeled by a unique angle $\theta = 2\pi(m-1)/M$, where $1 \le m \le M$. In this "ring model," the interaction between populations θ and θ' depends on $\theta - \theta'$ and is given by: $W(\theta,\theta') = J_0 + J_2 \cos(\theta - \theta')$, where J_0 represents a global uniform coupling and J_2 is the magnitude of the spatial interaction (5).

In stimulus condition, all neurons from population θ receive an external input I_θ that is broadly tuned around θ^* and is taken as:

$$I_\theta = C\left[1 - \varepsilon + \varepsilon \cos(\theta - \theta^*)\right]. \qquad \textbf{[S9]}$$

The parameter ε represents the degree of angular anisotropy (fixed to 0.1) of the input and C is associated to the stimulus contrast.

Augmented Moment Method. We used the Augmented Moment Method (AMM) (6, 7) to express the system of stochastic differential Eqs. **S4–S6** in terms of three moments of the distribution of rate variables: μ, the expected mean population firing rate; γ, the averaged fluctuations of the firing rates of the neurons of a given population; ρ, averaged mutual correlation between pairs of neurons. The moments are defined as:

$$\mu^m(t) = \langle R^m(t) \rangle = \frac{1}{N_m} \sum_i \langle r_i^m(t) \rangle, \qquad \textbf{[S10]}$$

$$\gamma^m(t) = \frac{1}{N_m} \sum_i \left\langle \left[r_i^m(t) - \mu^m(t) \right]^2 \right\rangle, \qquad \textbf{[S11]}$$

and

$$\rho^{mn}(t) = \frac{1}{N_m N_n} \sum_i \sum_j \left\langle \left[r_i^m(t) - \mu^m(t) \right] \left[r_j^n(t) - \mu^n(t) \right] \right\rangle. \qquad \textbf{[S12]}$$

Using the AMM deterministic equations of motion of the moments can be obtained. Briefly, this method uses the Fokker–Plank equation to derive equations for $\langle r_i^m \rangle$ and $\langle r_i^m r_j^n \rangle$; then, Taylor expanding r_i^m around μ^m—that is, $r_i^m = \mu^m + \delta r_i^m$—and keeping the terms up to $\langle \delta r_i^m \delta r_j^n \rangle$, the equations of motion of the moments are derived:

$$\frac{d\mu^m}{dt} = -\mu^m + H(u_m), \qquad \textbf{[S13]}$$

$$\frac{d\gamma^m}{dt} = -2\gamma^m + 2\frac{\partial H(u_m)}{\partial u} \left[\frac{N_m w_{mm}}{N_m - 1} \left(\rho^{mm} - \frac{\gamma^m}{N_m} \right) + \frac{1}{M-1} \sum_{n \neq m} w_{mn} \rho^{mn} \right] + \left(\beta_I \frac{\partial H(u_m)}{\partial u} \right)^2 + \beta^2, \qquad \textbf{[S14]}$$

$$\frac{d\rho^{mn}}{dt} = -2\rho^{mn} + \frac{\partial H(u_m)}{\partial u} \left[w_{mm} \rho^{mn} + \frac{1}{M-1} \sum_{k \neq m} w_{mk} \rho^{nk} \right] \frac{\partial H(u_n)}{\partial u} \left[w_{nn} \rho^{mn} + \frac{1}{M-1} \sum_{k \neq n} w_{nk} \rho^{mk} \right] + \frac{1}{N_m} \left(\beta^2 + \beta_I^2 \left(\frac{\partial H(u_m)}{\partial u} \right)^2 \right) \delta_{mn}, \qquad \textbf{[S15]}$$

and

$$u_m = w_{mm} \mu^m + \frac{1}{M-1} \sum_{n \neq m} w_{mn} \mu^n + I_m. \qquad \textbf{[S16]}$$

Note that the equations for γ and ρ are coupled and depend on the derivative of the transfer function and the connectivity, and thus are shaped by network interactions. Note that for strongly inhibited populations the derivative of the transfer function is null and the variance is dominated by the additive noise—that is, for these populations, the network does not amplify the noise.

The level of correlation inside a given population can be expressed by the synchronization ratio that is obtained by defining first the quantity:

$$P^m(t) = \frac{1}{N_m^2} \sum_{i,j} \left\langle \left[r_i^m(t) - r_j^m(t) \right]^2 \right\rangle = 2[\gamma^m(t) - \rho^{mm}(t)]. \qquad \textbf{[S17]}$$

By comparing P^m with its expected value ${P_0}^m$ in the asynchronous state, for which $\rho^{mm} = \gamma^m/N_m$ and thus ${P_0}^m(t) = 2\gamma^m(t)[1-1/N_m]$, the synchronization is defined by:

$$S^m(t) = 1 - \frac{P^m(t)}{P_0^m(t)} = \frac{N_m \rho^{mm}(t)/\gamma^m(t) - 1}{N_m - 1}. \qquad \textbf{[S18]}$$

The quantity S^m is equal to zero in the asynchronous state, and it is equal to 1 in the completely synchronous state in which all neurons have the same firing rate $R(t)$ (6).

Simulations

Dynamical equations given by the AMM (Eqs. **S13–S15**) were numerically integrated using a fourth-order Runge–Kutta method with time step equal to 0.1. In direct simulations, the system of stochastic Eqs. **S4–S6** was integrated using the Euler's method with a time step of 0.05. To mimic slow ongoing fluctuations in direct simulations, the input noise is an exponentially filtered white noise, with zero mean and deviation σ, defined by the following Ornstein–Uhlenbeck equation:

$$\tau_n \frac{dn_i(t)}{dt} = -n_i(t) + \sqrt{\sigma} \xi_i(t), \qquad \textbf{[S19]}$$

where $\tau_n = 1$ s and $\xi_i(t)$ is uncorrelated Gaussian noise with mean equal to zero and unit variance.

In direct simulations of the stochastic system, to prevent negative values of the firing rate, which could arise from additive noise, we assumed that Eq. **S4** represents rate deviations from a baseline rate $r_0 = 1$ Hz.

FI. To quantify the encoding accuracy of the population response, we used the FI. Assuming that the network response is well

described by a multivariate Gaussian distribution, FI can be written as the sum of two terms: $FI = FI_{mean}+FI_{cov}$ (8), where:

$$FI_{\text{mean}} = f'(\theta)^T Q(\theta)^{-1} f'(\theta) \quad \textbf{[S20]}$$

and

$$FI_{\text{cov}}(\theta) = \frac{1}{2}\,\text{Trace}\left(\left[Q'(\theta)Q(\theta)^{-1}\right]^2\right), \quad \textbf{[S21]}$$

where $f(\theta)$ and $Q(\theta)$ are the tuning function and the covariance matrix evoked by a stimulus of direction θ, respectively; $f'(\theta)$ and $Q'(\theta)$ are the first derivatives with respect to the stimulus direction; and Z^T is the transpose of Z. Note that, because the ring network is rotation-invariant, FI, FI_{mean}, and FI_{cov} are the same for every θ.

Modeling the Dynamics of Variability Through Pre-Excitation. As shown in Fig. 1*A*, the FF of MT direction-selective neurons first decreased after application of the visual stimulus and then evolved to a function of stimulus direction. In this section, we tested whether the computational model can explain the dynamics of the FF consisting of (*i*) a sudden nonselective reduction compared with the spontaneous level, followed by (*ii*) a tuning of the variability according to stimulus direction. Previous studies (9, 10) have proposed that a change in the field of view drives the initial early phasic response of neurons from visual areas 17/18, which later represents specific features of the visual scene. Following these studies, we studied the effect on the trial-by-trial variability of a transient nonselective stimulus, followed by a stimulus with a particular direction. Specifically, initially all neurons from all neural population received the same input, $I_\theta = I_0$, corresponding to the spontaneous period; at time t = 0, the input is augmented equally for all neural populations—that is, $I_\theta = I_0+\Delta I$ (pre-excitation period); finally all neurons from population θ receive an external input I_θ that is broadly tuned around θ^* and is given by Eq. **S9** (directed stimulus period). All network and noise parameters were the same used in Fig. 5. Fig. S6 shows the response of the network to these consecutive inputs, when the network is in the homogeneous and marginal phases, respectively. In both cases, all neural populations elevated their firing rate before settling into a bump attractor representing the direction of the stimulus (Fig. S6 *A* and *B*). Note that the early elevation of the firing rate (first ∼50 ms after stimulus onset) is independent of stimulus direction (Fig. S7, see also Fig. S1*A*). During the phasic response, the FF is strongly decreased for all neural populations before presenting a tuning in response to the directed stimulus (Fig. S6 *C* and *D*), mimicking the time evolution of the profile of FFs similar to one observed experimentally (Fig. S6 *E* and *F*).

An alternative possibility is that the temporal evolution of neural responses results from internal dynamics. Internal dynamics might be governed by single-cell and network features that are not considered in our simple model, such as adaptation, short-term synaptic plasticity, excitation–inhibition delays, specific channel dynamics, and complex interaction between sensory inputs and ongoing dynamics. All these possible mechanisms are not present in our simple model, wherein simple (first-order) dynamics limits the investigation of nonstationary transients.

1. Movshon JA, Adelson EA, Gizzi M, Newsome WT (1985) The analysis of moving visual patterns. *Study Group on Pattern Recognition Mechanisms*, eds Chagas C, Gattass R, Gross CG (Pontifica Academia Scientiarum, Vatican City, Italy), pp 117–151.
2. Pelli DG, Zhang L (1991) Accurate control of contrast on microcomputer displays. *Vision Res* 31(7-8):1337–1350.
3. Thiele A, Dobkins KR, Albright TD (2000) Neural correlates of contrast detection at threshold. *Neuron* 26(3):715–724.
4. Thiele A, Dobkins KR, Albright TD (2001) Neural correlates of chromatic motion perception. *Neuron* 32(2):351–358.
5. Ben-Yishai R, Bar-Or RL, Sompolinsky H (1995) Theory of orientation tuning in visual cortex. *Proc Natl Acad Sci USA* 92(9):3844–3848.
6. Hasegawa H (2003) Dynamical mean-field theory of spiking neuron ensembles: Response to a single spike with independent noises. *Phys Rev E Stat Nonlin Soft Matter Phys* 67(4 Pt 1):041903.
7. Hasegawa H (2009) Population rate codes carried by mean, fluctuation and synchrony of neuronal firings. *Physica A* 388(4):499–513.
8. Abbott LF, Dayan P (1999) The effect of correlated variability on the accuracy of a population code. *Neural Comput* 11(1):91–101.
9. Eriksson D, Valentiniene S, Papaioannou S (2010) Relating information, encoding and adaptation: Decoding the population firing rate in visual areas 17/18 in response to a stimulus transition. *PLoS ONE* 5(4):e10327.
10. Roland PE (2010) Six principles of visual cortical dynamics. *Front Syst Neurosci* 4:28.

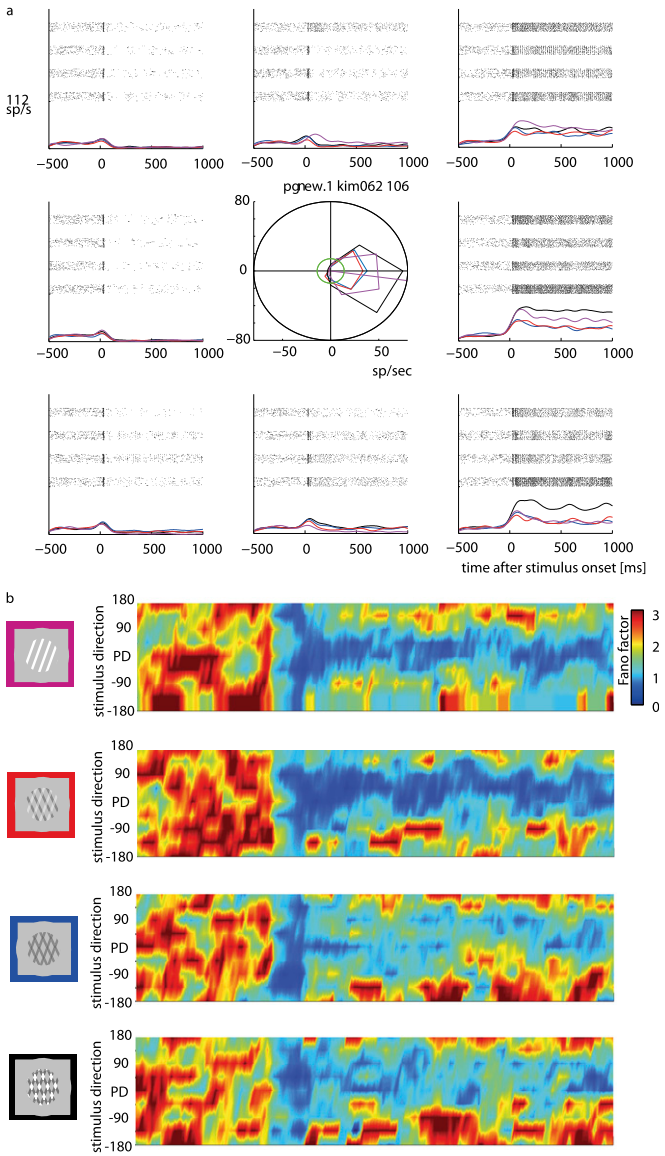

Fig. S1. Neuronal activity and time-resolved FF of an example cell. (*A*) The different subplots show neuronal activity and peristimulus time histogram (PSTH) for the stimuli moving in different directions. Each subplot contains four different raster plots, which show the activity for grating stimuli (*Top*, magenta PSTH), depth ordered plaids (*Upper Middle*, red PSTH), noncoherent plaid (*Lower Middle*, blue PSTH), coherent plaid (*Bottom*, black PSTH). The center plot shows the stimulus-dependent tuning curves. The green circle indicates baseline activity level. The red pointer shows the PD for the grating stimulus based on vector average calculation. (*B*) Time-resolved FF (color coded) for the different stimulus types (symbols on the left). The color under each symbol refers to the neuronal activity shown on the histograms and center direction tuning plot in *A*. The *y*-axis indicates which stimulus direction was presented; the *x*-axis shows time after stimulus onset. FF was calculated in a sliding window of 100 ms length (*Methods*). The color bars show the values of FFs.

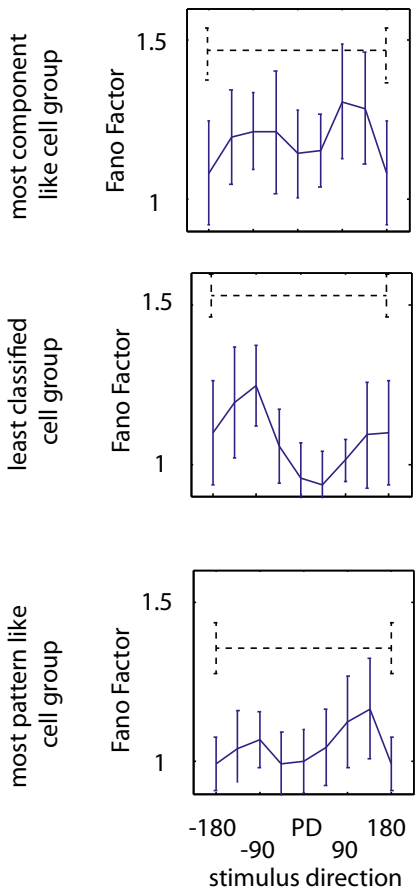

Fig. S2. FF tuning for different cell types. Averaged FF (±SEM) for different cell types (top to bottom) calculated within the time window from 150 to 400 ms after stimulus onset relative to preferred motion direction (PD). The dashed line shows average (±SEM) of FF before stimulus onset.

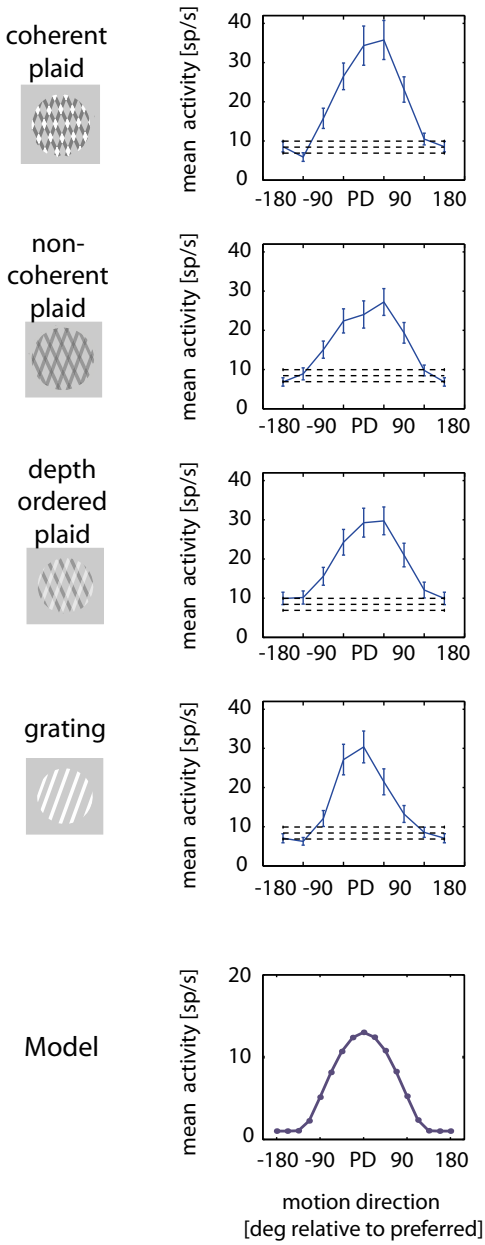

Fig. S3. Nonnormalized population activity. Tuning of MT neuronal population to different stimulus directions (plotted along *x*-axis). The figure shows population mean activity (*y*-axis) when coherently moving plaids (*Top*), noncoherent plaids (*Upper Middle*), depth ordered plaids (*Lower Middle*), and gratings (*Bottom*) were presented (the different stimuli are shown as cartoons on the left). The dashed line shows mean baseline activity (±SEM), measured during the 500 ms period before stimulus onset. For comparison, the model tuning curve is replicated here (*Bottom*; same model parameters as for Fig. 5*B*, $J_0 = -40$, $J_2 = 32$, $C = 3$, $I_0 = 2$, $\beta = 0.01$, $\sigma = 0.3$, $n = 20$, $M = 16$).

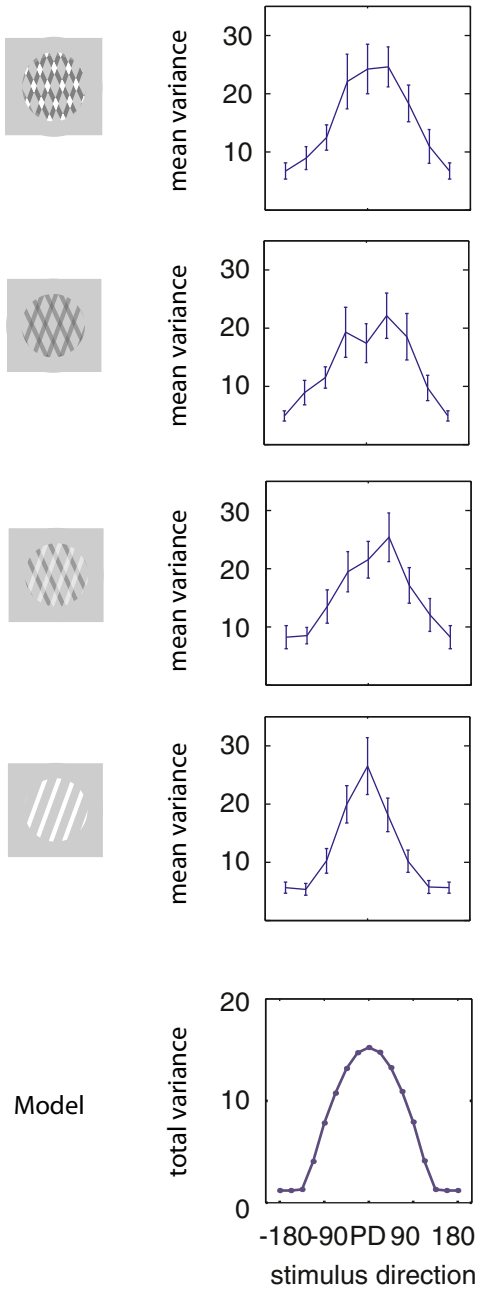

Fig. S4. Nonnormalized variance. Tuning of activity variance for the MT neuronal population in response to different stimulus directions (plotted along *x*-axis). The figure shows population mean variance (*y*-axis) when coherently moving plaids (*Top*), noncoherent plaids (*Upper Middle*), depth ordered plaids (*Middle*), and gratings (*Lower Middle*) were presented (the different stimuli are shown as cartoons on the left). (*Bottom*) Total variance of the model (i.e., underlying rate variability plus the expected Poisson variance). Same model parameters as for Fig. 5*B*, $J_0 = -40$, $J_2 = 32$, $C = 3$, $I_0 = 2$, $\beta = 0.01$, $\sigma = 0.3$, $n = 20$, $M = 16$.

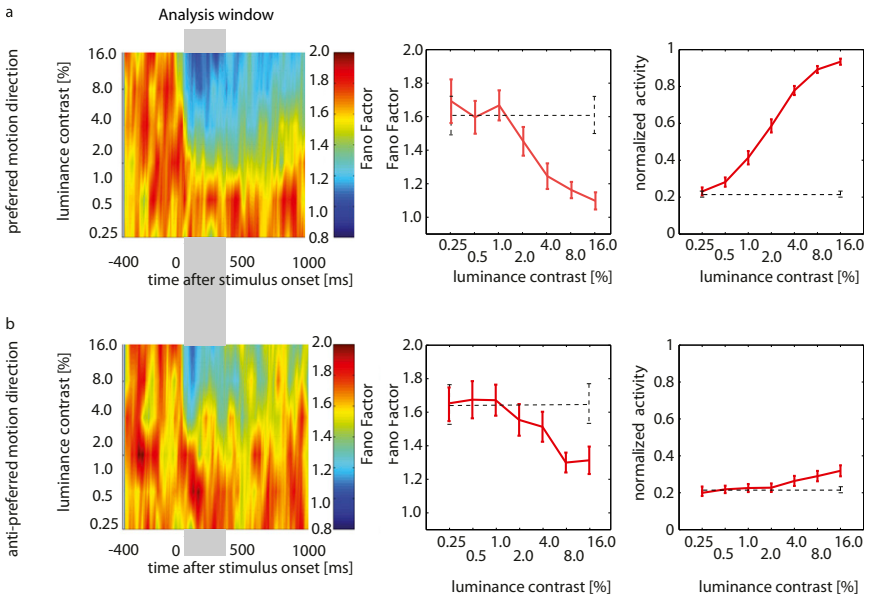

Fig. S5. Tuning of FFs for different stimulus contrasts. (*A*, *Left*) Time-resolved population FFs, indicated by color coding, for the preferred motion and different stimulus contrasts [preferred motion (upper row), replotted here from Fig. 1 to allow for comparison against and antipreferred motion (lower row)] plotted along the *y*-axis within each row. FFs were calculated in sliding windows of 100 ms shifted in 10 ms steps. (*Center*) Averaged FF (±SEM) for different stimulus contrasts, calculated within the analysis time window indicated by the gray horizontal bar in the *Left* panel. The dashed line shows average (±SEM) of FF before stimulus onset. (*Right*) Normalized mean firing rate (±SEM) for the different stimulus contrasts. The dashed line shows average (±SEM) of activity before stimulus onset. (*B*) Same as in *A* but for antipreferred motion direction. (*Left*) Time-resolved population FFs for the antipreferred motion and different stimulus contrasts. (*Middle*) Averaged FF (±SEM) for the different contrasts of the antipreferred stimulus, calculated within the analysis time window. The dashed line shows average (±SEM) of FF before stimulus onset. (*Right*) Normalized mean firing rate (±SEM) for the different contrasts of the antipreferred stimulus. The dashed line shows average (±SEM) of activity before stimulus onset.

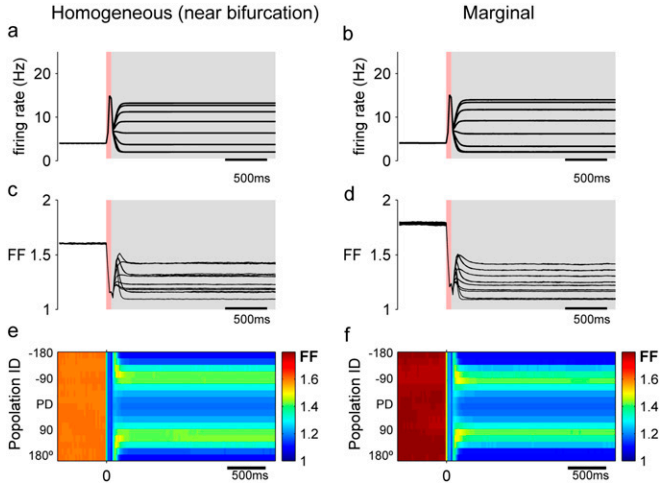

Fig. S6. Dynamics of FF. The time evolution of network response to a transient nonselective stimulus, followed by a directed stimulus, when the network is in the homogeneous (*A*, *C*, and *E*) and marginal (*B*, *D*, and *F*) phases. (*A* and *B*) The transient nonselective (same for all neural populations) stimulus elevates the firing rate of all neurons (red period), whereas the subsequent directed (gray period) stimulus breaks the symmetry and drives the network into a bump attractor. (*C* and *D*) The FF is strongly reduced in all neural populations after application of the nonselective stimulus and evolves to a function of stimulus direction during application of the directed stimulus. (*E* and *F*) FFs for each neural population, ordered by direction selectivity. Parameters in *A*, *C*, and *E*, $J_0 = -40$, $J_2 = 32$. Parameters in *B*, *D*, and *F*, $J_0 = -40$, $J_2 = 33$. Other parameters, $I_0 = 2$, $\Delta I_0 = 11$, $C = 3$, $\beta = 0.01$, $\sigma = 0.3$, $n = 20$, $M = 16$.

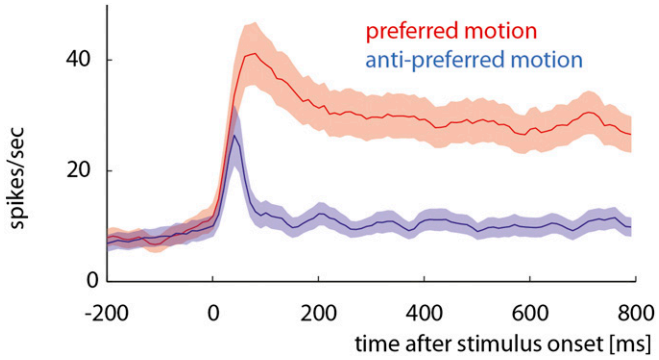

Fig. S7. Time-resolved mean activity. The PSTH for the population of recorded neurons for the stimuli moving in preferred and antipreferred motion direction. Colored areas indicate ±SEM. The figure shows the data for grating stimuli.